Thin-Film Stabilization of a Ferroelectric Orthorhombic α-Pr2 WO6 Polymorph

Mégane Lheureux, Marie-Hélène Chambrier, Kevin Dalla Francesca, Beatriz Vargas, Lluis Yedra, Antonio Da Costa, Thomas Carlier, Florent Blanchard, Sonia Estradé, Francesca Peiro, et al.

Thin film stabilization of a ferroelectric orthorhombic α-Pr_2WO_6 polymorph

Mégane Lheureux [a], Marie-Hélène Chambrier [a], Kevin Dalla Francesca [a], Beatriz Vargas [b], Lluis Yedra [b], Antonio Da Costa [a], Thomas Carlier [a], Florent Blanchard [c], Sonia Estradé [b], Francesca Peiro [b], Pascal Roussel [c], Jean-François Blach [a], Anthony Ferri [a], Rachel Desfeux [a]*

[a] Univ. Artois, CNRS, Centrale Lille, Univ. Lille, UMR 8181 – UCCS – Unité de Catalyse et Chimie du Solide, F-62300 Lens, France

[b] LENS, MIND-IN2UB, Department of Electronics and Biomedical Engineering, Universitat de Barcelona (UB), Martí i Franquès 1, Barcelona, 08028, Spain.

[c] Univ. Lille, CNRS, Centrale Lille, Univ. Artois, UMR 8181 – UCCS – Unité de Catalyse et Chimie du Solide, F-59000 Lille, France

* Corresponding author: mhelene.chambrier@univ-artois.fr

KEYWORDS. Thin film stabilization, Pulsed Laser Deposition, α-Pr_2WO_6 polymorph, Microstructural studies, Nanoscale ferroelectricity.

Abstract

An orthorhombic α-Pr_2WO_6 (PrWO) polymorph with a = 16.57(5) Å, b = 5.52(5) Å and c = 8.73(1) Å, isostructural to α-La_2WO_6 and α-Nd_2WO_6, has been stabilized in the form of thin film by pulsed laser deposition on (001)-oriented $SrTiO_3$ substrates. Combining X-ray diffraction pole-figure measurements and transmission electron microscopy (TEM) analysis, the c-axis films gave evidence of the orientations $[100]_{PrWO} \parallel [110]_{STO}$ and $[010]_{PrWO} \parallel [1\bar{1}0]_{STO}$

in the plane. Advanced φ-scans and reciprocal space mapping characterizations confirm the existence of the orthorhombic ($Pm2_1n$) structure in the film in place to the tetragonal one as also suggested. X-ray thermodiffraction measurements highlight the stability of this polymorph in thin film up to 900°C at least. Optical measurements performed by spectroscopic ellipsometry reveal that the band gap in such 36 nm-thick films (as confirmed by both X-ray reflectivity and TEM measurements) is 2.5 eV. Besides, the local piezoelectric hysteresis loops recorded by using the spectroscopic tool of the piezoresponse force microscopy attest to the robustness of the piezoelectricity and ferroelectricity in these α-Pr_2WO_6 films. This study demonstrates the existence of a new lead-free ferroelectric material in the series of the α-Ln_2WO_6 (lanthanide) tungstates, which can be considered as a promising candidate for applications in both nanoelectromechanically and energy harvesting systems as well as for integrating optics.

INTRODUCTION

Lead-free ferroelectric materials have been increasingly investigated in the last twenty years, both in bulk and thin film, due to European Union legislations and REACH (*Registration, Evaluation, Authorization and Restriction of Chemicals*) classifications which require the management, the restriction and the eradication of toxic substances, *i.e.* lead, from equipment in order to reduce their impact on the environment and health. [1, 2, 3] To date, the most popular materials which have been studied are $BaTiO_3$ (BT) including $(Ba,Ca)(Zr,Ti)O_3$ (BCTZ) based-BT oxides, $KNbO_3$-$NaNbO_3$ (KNN) solid solutions and $Bi_{0.5}Na_{0.5}TiO_3$ (BNT) including BNT-BT compounds. [4, 5, 6, 7, 8, 9] In this list of materials, we must mention multiferroic $BiFeO_3$ (BFO) and bismuth ferrite-based materials, that have been more recently studied extensively for their possible coupling between ferroelectric and magnetic ordering at room temperature and thus for their potential revolutionary technological applications. [10, 11, 12]

In parallel to the investigations performed on these metal oxide materials crystallized in the perovskite-based structure, other innovative families of ferroelectric materials with specific structures emerged, keeping in mind the compounds have to be non-centrosymmetric, along with a spontaneous and switchable polarization, to be proper ferroelectric. [13, 14] For about ten years in our lab, we have been interested in ~~to~~ the rich A_2O_3-MO_3 (A = Bi and rare earth, M = Mo or W) system for functional properties (electrical, catalytic…), and more specifically in Ln_2WO_6 lanthanide tungstates for ferroelectric properties in thin films. [15, 16, 17] In 2015, we revealed the existence of ferroelectricity in La_2WO_6 (LaWO) thin films epitaxially grown on (001)-oriented $SrTiO_3$ (STO) substrates. [15] We especially showed that strains induced by the substrate in the film stabilized the high-temperature orthorhombic α-phase at Room Temperature (RT), usually found in bulk at temperature higher than 1430°C while Piezoresponse Force Microscopy (PFM) measurements highlighted the ferroelectric nature of the film. [15] In 2016, we confirmed these results by deposition of $LaWO_6$ on (001)-oriented $LaAlO_3$ (LAO) substrates. [16] Next, we were interested in the Nd_2WO_6 (NdWO) compound which crystallizes in a tetragonal non-centrosymmetric crystalline class (hypothetic space group $P\bar{4}2_1m$) in bulk at high temperatures (T > 1450°C) as reported by Yoshimura *et al.*. [18] At RT, in bulk, this compound crystallizes in the centrosymmetric $C\frac{2}{c}$ space group, excluding ferroelectricity, while between 1430 and 1450°C, a metastable polymorph was described in the orthorhombic system with the acentric space group $P2_12_12_1$. [19] Very interesting, we showed in 2020 that it was possible to stabilize the α-NdWO polymorph on (001)-oriented STO substrates, isostructural to the orthorhombic high-temperature of bulk α-LaWO, although it does not exist in bulk form. Both piezo- and ferroelectricity were also demonstrated at RT in this newly discovered α-NdWO polymorph. [17]

In this paper, we propose to extend the study to the Pr_2WO_6 (called hereafter PrWO) oxide belonging to the Ln_2WO_6 family. Focusing on the Pr_2O_3-WO_3 system and to the best of our

knowledge, less than ten publications are dealing with this system due to the Pr^{3+} stabilization difficulties. [20, 21, 22, 23, 19, 24] Considering Efremov studies, from a structural point of view, PrWO in bulk behaves with varying temperatures as NdWO. [22, 19, 23] At RT, under air, it crystallizes in a monoclinic fluorine type-superstructure. As claimed by Yoshimura at high temperature around 1350°C, an orthorhombic metastable polymorph, quoted δ, is observed between 1430°C and 1450°C. [24] For temperatures higher than 1500°C, PrWO is expected to crystallize in the space group $P\bar{4}2_1m$ as NdWO with the cell parameters of a tetragonal structure slightly higher than $a \sim 5.3$ Å and $c = 8.5$Å when taking into consideration the higher ionic radius of Pr^{3+} ($r_{ionic}(Pr^{3+}[6]) = 0.99$ Å) compared to the one of Nd^{3+} ($r_{ionic}(Nd^{3+}[6]) = 0.983$ Å). Finally, PrWO melts congruently around 1675°C. **Figure 1** condenses the different polymorph structures for PrWO composition depending on the temperature.

In the present work, we grow PrWO thin films on (001)-oriented STO substrates by Pulsed Laser Deposition (PLD) and again for LaWO and NdWO. Advanced microstructural characterizations are led on the films by X-Ray Diffraction (XRD) and Transmission Electron Microscopy (TEM), while optical properties of PrWO films, leading to the determination of the film thickness as well as the band gap, are measured by Spectroscopic Ellipsometry (SE). Piezoresponse Force Microscopy (PFM) analyses were carried out on the films to locally probe piezo- and ferroelectricity in the films. We demonstrate that a new ferroelectric α-polymorph with orthorhombic structure at RT, *i.e.* α-PrWO isostructural to α-LaWO and α-NdWO, can be successfully stabilized in thin film form.

EXPERIMENTAL METHODS

A β-PrWO ceramic pellet, 1 inch in diameter and 5 mm-thick, was used as target for laser ablation. The ceramic was prepared by solid-state reaction route method, mixing dried oxides

Pr_6O_{11} and WO_3 (Sigma Adrich, purities of 99.9%) weighted in stoichiometric proportions. At 1200°C, and twice at 1350°C, the mixture with two intermediate grindings was heated for one night in air. The resulting powder was then ground, pressed to form a disc using an uni-axial press, sintered up to 1450°C for 12h in air and slowly cooled down to room temperature. The XRD pattern confirms the synthesis of a pure powder of the low temperature β-polymorph of PrWO that was afterward used as target for the deposition procedure. [25]

The depositions as thin films form by PLD were carried out with a Compex Pro 102 KrF excimer laser (λ = 248 nm) on commercial (001)-oriented STO single-crystal substrates (Crystal GmbH, Germany). The fluence was adjusted to 2 J/cm² and the deposition rate was 2 Hz. The target-substrate distance was adjusted to d = 4.5 cm. All substrates were first ultrasonically cleaned in ethanol for 5 minutes and then dried. The base pressure in the pulsed-laser chamber was lowered down to 10^{-4} Pa. Then, the substrate temperature was heated up at 10°C/min ramp rate to the growth temperature, *i.e.* 900°C under a dynamical O_2 pressure of 10^{-1} mbar. [15]

Depositions corresponding to 6000 laser-pulse shots were performed. Finally, at the end of deposition, O_2 gas pressure was increased up to 200 mBar inside the chamber and the film was slowly cooled down to room temperature.

The bulk-powder X-ray diffractograms were obtained using a Rigaku Ultima IV diffractometer equipped with a Cu-anode X-ray tube ($\lambda_{K\alpha}$ = 1.5418 Å) and a point detector. The thin films [indexation, rocking curves and Reciprocal Space Maps (RSMs)] were characterized using a Rigaku SmartLab X-ray diffractometer equipped with a 9 kW rotating copper anode. For 2θ-ω and rocking curves analysis as well as ϕ-scan and RSMs, a high-resolution configuration was used: the X-Ray beam was made parallel with a cross-beam optics and monochromatized with a double Ge (220) monochromator ($\lambda_{K\alpha}$ = 1.54059 Å). In this study, all the 2θ-ω scans were performed in the range 10-90°, with a 0.02° step size and a 1°/min

speed whereas the Φ-scan was acquired in the range of -10-360°, with a step size of 0.4° and a 40°/min speed. Pole figure measurements were made in medium resolution configuration, *i.e.* without the monochromator ($\lambda_{K\alpha}$ = 1.5418 Å) using an in-plane geometry.

A cross-sectional sample for Transmission Electron Microscopy (TEM) was prepared in a ThermoFischer Scios 2 DualBeam. Electron diffraction patterns and High Resolution (HRTEM) images were acquired in a JEOL 2010F TEM working at 200KV.

Spectroscopic Ellipsometry (SE) measurements were performed at RT using a phase-modulated ellipsometer (UVISEL HR460 from Horiba Scientific) at wavelengths ranging from 300 to 1500 nm with 2 nm interval and using an incidence angle of 70°.

The raw signal measured by SE has the following form: $I(t) = I_0 + I_S\, sin(\,\delta(t)) + I_C\, cos(\,\delta(t))$, where δ(t) is the phase shift of a modulator. In our experimental setup, the value of I_0, I_C and I_S are related to the ellipsometric angles (Δ, Ψ) by the following relations $I_0 = 1$, $I_s = \sin 2\psi \sin\Delta$, $I_c = \sin 2\psi \cos\Delta$. The ellipsometric angles Δ and Ψ are linked to the complex reflection coefficients in polarized light (R_p and R_s for respectively a polarization parallel and perpendicular to the plane of incidence) by the following relation: $\rho = \frac{R_P}{R_S} = tan\,\psi\, e^{i\Delta}$. For each sample, the measured spectrum was analyzed using an appropriate fitting model based on the sample structure. For this modeling, we created a virtual sample with the same number of layers (substrate, film layers, roughness). For each layer, we defined a thickness and the refraction index (in the case of the rough layers, the optical index was calculated by using the effective medium theory). This model allows the calculation of the ellipsometric angles ψ and Δ for each value of wavelength. The unknown parameters (optical index, thicknesses, percentage of void) were determined by finding the global minimum of a merit function χ^2 (Levenberg-Marquardt algorithm) which compares the ellipsometric angles obtained by the model with those obtained by the measurements (see **SI1**).

Atomic Force Microscopy (AFM) and PFM analyses for both surface morphology and local electrical properties were carried out with a commercial AFM microscope (MFP-3D, Asylum Research/Oxford Instruments) under ambient conditions. Pt/Ir-coated tip and cantilever with a stiffness of about 2.9 $N.m^{-1}$ were used. The dual AC resonance tracking (DART) mode of the PFM was employed in order to improve the detected piezoelectric signal. [26] Switching Spectroscopy PFM (SS-PFM) was conducted by applying a driving voltage V_{AC} of 1.5 V to the conductive AFM tip and by using the remnant mode. This allows the electrostatic contribution to be reduced in benefit of the electromechanical response. [27] For PFM measurements, semiconductive (001)-oriented Niobium doped (1.4 atom %) $SrTiO_3$ (Nb-doped STO) substrates were used.

RESULTS AND DISCUSSION

Structural characterizations

Structural characterizations have been performed by XRD and TEM in order to check not only the crystalline quality of the thin film but also its epitaxy relationships with the substrate, the mosaicity, the crystal system and also the lattice parameters. First of all, a 2θ-ω diffractogram of the as-deposited thin film was collected (**Fig.2a**). Two series of diffraction peaks were identified corresponding to the (001) oriented-STO substrate (in black) and the thin film (in red). The well-defined and intense diffraction peaks attributed to the film indicate a good crystallization of the deposited material. By reference to previous works conducted on LaWO and NdWO thin films, [15,17] the present PrWO X-ray diffractogram shows several common points, suggesting that the growth of PrWO in thin film by PLD leads to the stabilization of the "α-LaWO" structure type despite the target used for deposition is the β-PrWO low-temperature polymorph. As a reminder, the α-LaWO type structure is referenced as the bulk high-temperature orthorhombic LaWO polymorph that adopts the non-

centrosymmetric space-group $Pm2_1n$ with the following cell parameters $a_{LaWO} \approx 16.56$ Å, $_{bLaWO} \approx 5.52$ Å and $c_{LaWO} \approx 8.89$ Å. [28] Starting from this hypothesis, the identification of PrWO X-ray diffraction peaks could be achieved. Three different peak families have been identified: the most intense ones, as observed previously on La and Nd based films, are indexed as 00***ℓ*** peaks indicating a privileged growth along the *c*-direction. Other peaks, less intense, are also observed and are related to other directions: the 510 one, already observed only for NdWO and finally, the 0k0-familly with the *b*-axis perpendicular to the plane of the substrate. Several attempts were tried to stabilize a single 00l-oriented thin film, but, probably because of the increasing refractory character of the Ln^{3+} with ionic radius, highest temperature than our technical limit of 900°C would have been needed. In fact, the thermal energy *i.e.* the substrate temperature during growth, appears be a key parameter to obtain high-quality (00l)-heteroepitaxial films keeping in mind that a lower temperature than the optimized one leads to poorly crystallized films along with the existence of other crystallographic orientations with respect to the plane of substrate as observed for LWO and NdWO oxides. [15;17] However, we cannot exclude that other parameters such as interfacial energies between the lanthanide tungstate and the substrate or/and electron nature of the lanthanide also play a role on the growth of the LnWO compound.

Nevertheless, some interesting structural features have been extracted from those data: the *c*-parameter was accurately calculated to 8.73 Å considering the seven 00***ℓ*** harmonic diffraction peaks. This value can be compared to those measured for the LaWO and NdWO thin films grown on (001)-oriented STO substrates, with c-parameters *i.e.* 8.87(5) Å and 8.68(1) Å, respectively, in good agreement with the evolution of the Ln^{3+} radius, considering that the three compounds crystallize in the same α-type polymorph. **Fig.3,** in red, shows the evolution of the thin film *c*-cell parameter with the Ln^{3+} ionic radius ($Ln^{3+} = La^{3+}$, Pr^{3+} and Nd^{3+}) (from Shannon *et al.* values), [29] considering a six-fold coordinate, as observed in average for bulk α-LaWO.

Fig.3 reports also the linear dependence of the *c*-cell parameter for bulk α-HT Ln_2WO_6 [see also **SI.2**] by reference to Yoshimura's works. [30] Very closed values are obtained between c-cell parameter for the bulk and the thin film even if as thin film Ln_2WO_6 is constrained. Considering that the (001)-oriented STO substrate used is unchanged, the balance between constraints and Ln^{3+} ionic radius dependence, i.e. Ln_2WO_6 cell volume decreases when $r_{Ln^{3+}}$ decreases, is varying and could explain the apparition of several oriented domains in order to relax the increasing strains that would occur.

To check the thin film crystalline quality, by comparison to the Nb-doped STO single-crystal substrate, some rocking-curve measurements (**Fig. 2b**) were done on both the 002-peak of the PrWO thin film and the 001-peak of the Nb-doped STO substrate. The full-width at half maximum (FWHM) value obtained for PrWO is around 0.13° compared to 0.07° for the STO substrate. The FWHM result for the PrWO thin film indicates a quite low mosaicity while a good crystallinity is observed.

As observed in the case of NdWO, the 2θ-ω X-ray diffractogram obtained for PrWO suggests a stabilization, as a thin film, of the *β*-orthorhombic polymorph. To verify this hypothesis and to extract more information on the in-plane direction, thin film φ-scans on the 101 and 011 reflections, in the case of orthorhombic symmetry have been acquired (**Fig. 4**). As already discussed in our previous works, [15, 17] these reflections are chosen because of both a non negligible intensity and a favorable position ($2\theta_{Bragg} \sim 19.2°$, χ angle between 001 and 101 plane is around 59.3°) is quite isolated from substrate ones.

Four peaks are observed as expected both for tetragonal and orthorhombic symmetries. The angular gap between two consecutive peaks is 89° or 91° while the angular gap between two peaks of the same family *i.e.* {101} and {011} is exactly 180°. These results are good indices of the crystallization of the PrWO thin film in an orthorhombic symmetry rather than a tetragonal one. Indeed, the latter system is characterized by the presence of an axis of a fourth-

order, and would lead to an angular gap of precisely $\frac{2\Pi}{4}$ between planes belonging to the same family. Note also that peaks on the φ-scans are quite intense showing that the in-plane crystalline quality of the film is quite good. Moreover, the peaks are not split, indicating that there is no strong misorientation of the coherent X-ray domains in the (101) and (011) plane.

To get a better insight on the structural properties of the PrWO film, some Reciprocal Space Maps (RSM) were recorded. Firstly, RSM around the [521]* (2θ = 44.400°, d = 2.0337Å and χ = 76.471°) reflection were acquired in order to check the existence of the orthorhombic structure of the film. Secondly, RSM measurements were led on the [301]* and [011]* reflections to accurately locate the position of the peaks and thus calculate the *a* and *b*-cell parameters adopted by the PrWO thin film grown on the 001-oriented Nb-doped STO substrate. Finally, a RSM combining thin film and substrate around both the [002]* reflection of *α*-PrWO and the [001]* reflection of STO has been recorded to observe if the domains are clamped or relaxed on the substrate. **Figure 5a** presents the existence of the [521]* node then confirming that the film crystallizes in the orthorhombic cell, as demonstrated for NdWO in our previous works. [15, 17] By levering the PLD technique for growing such PrWO film, starting from an *β* low-temperature polymorph target, we stabilized a new orthorhombic high-temperature of this composition, isostructural to the high-temperature *α*-LaWO polymorph and the *α*-NdWO one. The *a* and *b* parameters of the film were extracted from the 2*θ*-values measured on the RSM around the [301]* and [011]* reflections respectively. From the value of the c-lattice parameter deduced from the 2θ-ω diffractogram, we found *a* = 16.57 Å and *b* = 5.52 Å for the lattice parameters of the PrWO thin film. By comparison to the LWO (*a* = 16.57(5) Å, *b* = 5.72(5) Å; *c* = 8.87(1) Å; V = 840.19 Å^3) and NdWO (*a* = 16.34(1) Å, *b* = 5.46(1) Å; *c* = 8.68(1) Å, V = 774.40 Å^3) cell-parameters, the PrWO cell-volume is 798.50 Å^3. Once again, the calculated cell volume of PrWO, between the ones of LWO et NdWO, is in good agreement with the fact

that Pr is between La and Nd in the periodic table and the bulk LnWO volume evolution evocated by Brixner's and Yoshimura's works. [30,21]

The calculated cell-parameters and pole-figure open the way to have an idea of the constraints on the film induced by the substrate. In this way, the epitaxial relationships between film and substrate were first investigated through a pole-figure measurement on the 315 node of film.

As justified above, this 2θ position allows both the reflection 315 of the thin film and the reflection 112 of the substrate to be observed in the same measurement. By the simulation, using the Stereopole software, [31] and the comparison between the observed and calculated density of poles, we could deduce that the PrWO thin film adopts the following epitaxial relationships: $[100]_{PrWO}$ // $[110]_{STO}$, $[010]_{PrWO}$ // $[1\bar{1}0]_{STO}$ and $[001]_{PrWO}$ // $[001]_{STO}$ *i.e.* the same 3-D heteroepitaxy as α-LWO and α-NdWO when grown on (001)-oriented STO or LAO substrate.

Finally, considering a_{STO} = 3.905 Å for commercial STO substrates (Crystal GmbH) as well as and a_{PrWO} = 16.57 Å and b_{PrWO} = 5.52 Å by referencing to the results previously found in this paper from RSM, the epitaxial deformation ε and ε' between the film and the substrate can be calculated as follows:

$$\varepsilon = \frac{3a_{STO} \times \sqrt{2} - a_{PrWO}}{3a_{STO} \times \sqrt{2}} \times 100 \qquad \text{Equation [1]}$$

$$\varepsilon' = \frac{a_{STO} \times \sqrt{2} - b_{PrWO}}{a_{STO} \times \sqrt{2}} \times 100 \qquad \text{Equation [2]}$$

The value of epitaxial deformation for the direction $\overrightarrow{a_{PrWO}}$ is equal to ε = 1.8 % whereas for the $\overrightarrow{b_{PrWO}}$ is ε' = 0.72%. These low positive epitaxial deformations are indicating low tensile strains out of growth direction. Along with a high Curie temperature, such a PrWO thin film with low epitaxial deformations appears to be a good candidate for applications in extreme environment for sensor and actuator applications. In our previous work, [15,17] the lattice mismatches δ were calculated by comparison with powder high-temperature α-LnWO (Ln = La^{3+} or Nd^{3+}). In the present PrWO case, it is not possible to use the same approach since the

high-temperature PrWO compound in bulk has not yet been isolated. However, as given by Yoshimura's works, the *a*-and *c*-cell parameters evolution for LaWO, CeWO and NdWO, for Ln^{3+} in coordinance 6 show a linear evolution. [18] If we assume that such a tendency is also true for Pr compounds, the a and *c* cell parameters could be estimated around *c* ~ 8.72 Å and *a* ~ 5.42 Å for this hypothetic high-temperature tetragonal PrWO polymorph (**SI2**).

The hypothetical lattice mismatch δ can thus be calculated following the equation [3] and leads to a value around 1.9 %:

$$\delta = \frac{3a_{STO} \times \sqrt{2} - 3b_{PrWO}}{3a_{STO} \times \sqrt{2}} \times 100 \qquad \textit{with } b_{\mathrm{PrWO}} = 5.42 \text{ Å} \qquad \text{Equation [3]}$$

The simulated lattice mismatches δ and δ' are the same for a_{PrWO} and b_{PrWO} respectively, due to the tetragonal symmetry. It's interesting to note that the epitaxial deformation ε along $\vec{a}$ direction is around the value of the simulated lattice mismatch, whereas along $\vec{b}$ direction the epitaxial deformation ε' is two times weaker than δ, indicating an important adaptation of the thin film along this direction.

If we look at the parameter c, the one simulated in the tetragonal hypothesis evoked by Yoshimura, [18] is around 8.72 Å, as thin film we observed a value of 8.73 Å implying weak tensile constraints inside PrWO thin film. The comparison between the epitaxial deformation and lattice mismatches observed for LWO, NdWO and PrWO are summarized in table 1.

Table 1 :Evolution of lattice mismatches and epitaxial deformations for LaWO, PrWO and NdWO thin films grown by pulsed laser deposition

	LaWO	PrWO	NdWO		LaWO	PrWO	NdWO
Lattice mismatches (%)					**Epitaxial deformation (%)**		
δ	9.78×10^{-2}	1.9	1.7	ε	-0.151	1.8	1.33
δ '	4.53×10^{-2}			ε'	-3.57	0.72	1.09

The values are all under 2 %, indicating a quite good match between the film and the STO substrate. This is due to the close relationships between LnWO structures and STO ones: indeed, as discussed before, LnWO are related to scheelite-type structure, and $a_{Scheellite}$ is around $\sqrt{2}\, a_{STO}$. However, while the LaWO thin film is in compressive deformation and the other two on tensile one, PrWO thin film exhibits the maximal values of δ and ε of the three films. This observation could explain the occurrence of several growth directions observed on 2θ-ω XRD. Indeed, in the previous work on α-NdWO, [17] HRTEM evidenced a less important deformation in the 510-domains than in the 002 ones.

To have a better insight about the two other orientation domains, a large RSM between 25° and 45° has been performed for 2θ, as shown in **Fig.6**. Firstly, four reflections clearly appear in this angular range, at increasing 2θ, corresponding to [003]*, [510]*, [020]* and [004]*. Secondly, they are quite punctual and all are aligned along $\Delta\omega = 0°$, while no splitting is observed. This demonstrates both a single X'ray coherent domain (no twin) for all the out-of-plane orientation and a clamping on the (001)-oriented STO substrate.

Some *in situ* high-temperature XRD have been performed on the sample in order to assess both the thermal stability of the synthesized layer and also to compare it to the substrate thermal evolution. The sample was heated from 50 up to 900°C and subsequently cooled down to 50°C. The resulting diffraction patterns at different temperatures are shown in **Fig. 7**. Except the expected thermal dilatation, no thin film structural transition such as β-α transition is observed, indicating a high thermal domain stability for the PrWO thin film.

From those thermodiffraction results, the cell-parameter evolutions of both thin film and substrate were refined (**Fig. 8**), and the resulting thermal expansion coefficients (TEC) of the thin film and substrate along the c-axis direction were calculated. Obtained values are $\alpha_{PrWO} \sim 6.2\times10^{-6}\ K^{-1}$ and $\alpha_{STO} \sim 6.8\times10^{-6}\ K^{-1}$ indicating a slightly lower thermal expansion of the PrWO film compared to NdWO one's.

From these values a thermoelastic constrain close to 4.42×10^{-4} could be deduced from the equation [4] : [32]

$$\frac{\Delta c}{c} = \Delta T \times (\alpha(substrate) - \alpha(Thin\ film)) \quad \text{Equation [4]}$$

The film thickness was accurately evaluated using X-ray reflectivity technique (XRR). As reported **SI3**, clear oscillations were observed, evidencing a high structural quality for the film. Seven of these oscillations were used in order to give an estimation of the thickness.

At each oscillation (see **SI3b**), called Kiessing fringe, a portion of X-ray is reflected: there is a linear relation between the angular value of the m^{th} oscillation (θ_m) and the thickness (d), as shown by **Eq.5**:

$$\sin^2(\theta_m) = m^2\times(\frac{\lambda}{2d})^2 + \alpha^2_c \qquad \text{Equation [5]}$$

With θ_m: the angle of the m^{th} oscillation

m: the order of the oscillation

λ: the wavelengh (λ = 1.5418 Å)

d: the thickness

α_c: the critical angle, depending on the electronic density of the deposited materials

By picking several oscillation θ_i angles, it has been possible to determine a thickness around 38 nm.

Figure 9a shows several High-Resolution TEM (HRTEM) images of a cross-sectional sample of the thin film. The layer thickness was measured to be around 34 nm. The layer is completely crystalline while the presence of several grains is revealed (**fig.9b)** 1 (green highlighted) & 2 (yellow highlighted)). Upon closer observation, the interface with STO is flat and atomically sharp (**fig.9b)**. Considering the high-temperature polymorph α-LaWO structure for the thin film and STO structure for the substrate as references, it has been possible to determine the directions observed *i.e.* [010] for both the layer and STO:Nb substrate. The growth direction, as extracted from the indexed Fast Fourier Transforms (FFT), is [001] (**Fig. 10b and c**). The

comparison between the theoretical FFT (generated from CIF, **Fig. 10d** and **e**) and the experimental ones are in total accordance for the substrate and the [001]-PrWO oriented layer.

A HRTEM image (along a FFT of a selected area) and two nano beam electron diffraction patterns are presented in **Fig. 11 a-b** and **Fig. 11 c-d** respectively. The presence of satellite spots in the $[\bar{5}10]$ direction is noted in the FFT, indicating a superstructure at $\frac{1}{6}$. While the [001] orientation is preserved, the presence or absence of the satellites evidences a modulation parallel to the substrate surface organized in domains.

The sample PrWO deposited onto STO:Nb substrate was analyzed by spectroscopic ellipsometry (**Fig.12 a** and **c**). In order to obtain information on film thickness, we compared the experimental data with those obtained from a model (**Fig. 12a**). The model consists in the stacking of three virtual layers as represented in **Fig. 12b** scheme: a layer with a semi-infinite thickness as STO:Nb substrate (the optical function was extracted by a measurement performed on a pristine substrate); a dense layer of PrWO with an unknown thickness and finally a layer filled with a blend of PrWO and void for the simulation of the sample roughness (Bruggeman model). Concerning the optical function of PrWO (**Fig. 12c**), we used the "new amorphous" dispersion curve. The latter is interesting as we can include or extract some physical parameters such as the optical band gap. This optical function is described with the following coefficients extracted from the equations presented on **SI4.**

After the fitting procedure, we obtained the following results: thin film thickness d_1 = 36 nm ; roughness thickness d_2 = 22 nm; percentage of void in the roughness 19 % ; band gap wg = 2.5 eV; $n_\infty = 1$; $f_j = 0.58$; $\omega_j = 20.9\ eV$ and $\Gamma_j = 8.4\ eV$. It is worth to notice that the film thickness is close to the value obtained by TEM measurements (34 nm). Nevertheless, we can mention that we obtained a roughness thickness of 22 nm which is absent in TEM images; this difference occurs because the probe beam for ellipsometry is larger than the TEM electron beam, and can account for some surface defects not seen in the TEM region examined. Finally,

we can observe that this material is transparent for wavelengths above 500 nm and can be interesting for integrating optics. [33]

Nanoscale piezo-/ferroelectric properties

The surface morphology of the α-PrWO film is depicted in **Fig. 13a.** The AFM image reveals a nanostructured and rather smooth surface with a root mean square roughness of about 2.6 nm, as measured on a 20×20 μm² scan area. Square shaped grains with side lengths of about 300 nm are clearly observed. Such a specific morphology is different from thin films of α-LaWO and α-NdWO compounds previously observed, [15, 17] where dense nanometric rounded grains and irregular grains were obtained respectively.

SS-PFM experiments were performed over the free surface of the film to assess the piezo-/ferroelectric behavior at the nanoscale. For this purpose, measurements were achieved by positioning the AFM tip in the center of a hundred grains at different locations on the film surface and by simultaneously recording both amplitude and phase PFM loops. A small AC driving voltage was deliberately selected in order to be smaller than the ferroelectric coercive voltage, thus preventing detrimental polarization reversal under measurements. Representative piezoloops are displayed in **Fig. 13b**. Square hysteresis signal is obtained from the phase PFM response with two stable opposite polarization states. Corresponding amplitude loop shows a typical butterfly-like shape due to the converse piezoelectric effect. From the maximum deformation under positive and negative voltage excitation, we observed symmetric shapes evidencing the homogeneous piezoelectric properties of the stabilized films.

Nevertheless, it is worth noting that although such PFM loops are commonly attributed to nanoscale ferroelectric phenomena, this is not sufficient to definitively prove the ferroelectric polarization origin in the detected PFM signal for such complex oxides. [34] Indeed, the very high electric fields produced by the AFM tip can result in various physicochemical phenomena such as electrostatic or electrochemical effects. In order to exclude any parasitic origin of the

recorded PFM response, bias-dependent hysteresis experiments were conducted. First, the influence of the DC voltage on the PFM loops was assessed, as depicted in **Fig. 13c**. We noticed no significant change on the coercitive voltage in the loop area depending on the polarizing applied voltage when varying from 15 up to 25 V. This result excludes the ionic motion phenomena under the probing tip as the main factor to the electromechanical hysteresis response observed. [35] Then, the PFM loop dependence on the probing AC voltage with respect to the previously determined coercive voltage was studied, as reported in **Fig 13d**. Well-saturated phase loops showing a phase difference of almost 180° between the two polarization states were obtained when the driving voltage is lower than the coercive voltage (~4.3 V). In contrast, strong degradation of the loops occurs for applied AC voltages higher than the polarizing voltage coercivity, evidenced by both the progressive narrowing of the hysteresis and the reduction of the phase difference. This particular evolution of the PFM loops is attributed to the flipping of the ferroelectric polarization under measurements, affecting the recorded PFM signal at such high driving voltages. [36, 37] Such specific behaviors for the detected PFM signal are fully consistent with the dynamic of intrinsic polarization related to a ferroelectric polarization switching process. Consequently, the characteristic SS-PFM measurements presented in **Fig. 13b** can be ascribed to piezoelectricity and ferroelectricity occurring into our stabilized α-PrWO thin films. In addition, poling experiments were performed by locally manipulating the polarization of the domains *via* the application of DC electrical voltages of ±10 V through the AFM tip during scanning over the free surface of the film. Clear contrasts observed on both phase and amplitude PFM images reveal the efficiency of the local switching of the ferroelectric domains (see **Fig. SI5**). These results allow to assess both the ferroelectric switching voltage V_c and the effective piezoelectric coefficient d_{33}^{eff} of the stabilized PrWO layer. From the recorded phase PFM loops, an average coercive voltage characterizing the polarization reversal of ferroelectric domains of 4.3±0.5 V is determined,

indicating a reliable switching capability. The d_{33}^{eff} was then determined from the amplitude PFM loops by considering the formula $A = d_{33}^{eff} \times V_{AC} \times Q$, [17] where A is the deformation amplitude detected by PFM and Q the quality factor of the AFM cantilever related to the specific measurement at the cantilever contact-resonance frequency (DART-PFM method). Considering the experimental values for A, V_{AC} and Q of 300 pm, 1.5 V and *ca.* 100, respectively, d_{33}^{eff} is found to be around 2.0 pm/V. It is worth noting such a piezoelectric constant value locally determined cannot be taken into account as a pure quantitative value owing the strong inhomogeneous electric field produced by the AFM tip, the complicated calibration procedure and the relatively poor surface/tip contact. [38, 39] In addition, the film clamping to the substrate leads to an underestimated value, especially for such thin layers. Nevertheless, this estimated value for the piezo-activity opens up attractive perspectives in view of the development of advanced lead-free piezoelectrics based on the Ln_2WO_6 family.

CONCLUSION:

In summary, by pulsed laser deposition, the α-Ln_2WO_6 polymorph thin film family is enlarged to Pr_2WO_6. This compound was successfully stabilized at room temperature with a thickness around 36nm, as measured by using XRR, TEM and SE. The microstructural analyses revealed a well crystallized film with a predominant growth orientation along $\vec{c}$ direction. The interface substrate/film is quite smooth indicating a successfully heteroepitaxy. The cell parameters extracted from RSM and from HRTEM image FFT are: a = 16.57 Å, b = 5.52 Å and c = 8.73 Å. These values are in accordance with the previous results on LWO and NdWO thin films and the Ln^{3+} ionic radii. However, HRTEM images showed some structure modulation in plane even if the lattice mismatch and the stress values are not so important and the epitaxy relations are still the same from LWO and NdWO. The PrWO thin film is stable at

temperature higher than 900°C as evidenced by X-ray thermodiffraction with no anomalous TEC observed paving the way to the application in extreme conditions.

The optical function has been extracted from SE and the band gap could be estimated around 2.5 eV. The α-Pr_2WO_6 is transparent for wavelengths superior to 500 nm.

PFM analyses have clearly evidenced piezoelectricity and ferroelectricity at RT, particularly supported by advanced bias-dependent hysteresis experiments, making the new stabilized PrWO polymorph promising in a context of replacement of lead-based piezoelectric materials. Besides, to evaluate the application potential of these films, further measurements of dielectric permittivity and leakage currents are in progress

Supporting Information:

FIGURE S1: SPECTROSCOPIC ELLIPSOMETRY EQUATION $\boldsymbol{\chi^2}$

$$\chi^2 = min \sum_{i=1}^{n} \left[\frac{(\psi_{th} - \psi_{\exp})_i^2}{\sigma_{\psi,j}^{exp}} + \frac{(\Delta_{th} - \Delta_{\exp})_i^2}{\sigma_{\Delta,j}^{exp}} \right]$$

Where n is the number of measured Ψ and Δ pairs, $\sigma_{\psi,j}^{exp}$ and $\sigma_{\Delta,j}^{exp}$ are the standard deviations of $\Psi_{exp,i}$ and $\Delta_{exp,i}$. All fitting steps were performed using the Delta-Psi Horiba software (Horiba Scientific).

Figure S2: *a* and *c*-cell parameters of the tetragonal high-temperature α-Ln_2WO_6 (Ln = La, Ce and Nd) stabilized as a powder from Yoshimura results [30]

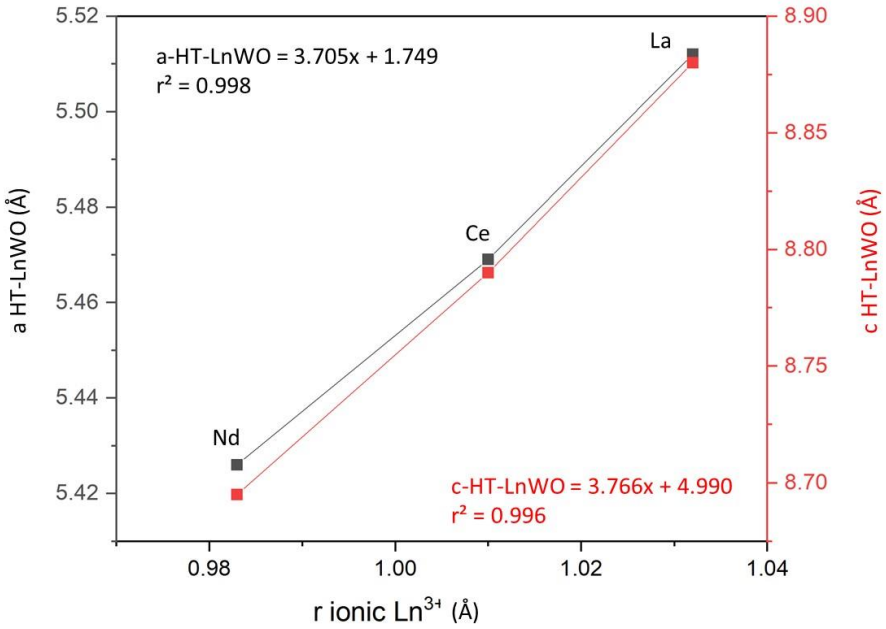

SUPPORTING INFORMATION

Figure S3: a) X-Ray reflectivity curve of α-PrWO thin film on STO-substrate; b) Evolution of $\sin^2\theta$ with m^2 the square period of the oscillation.

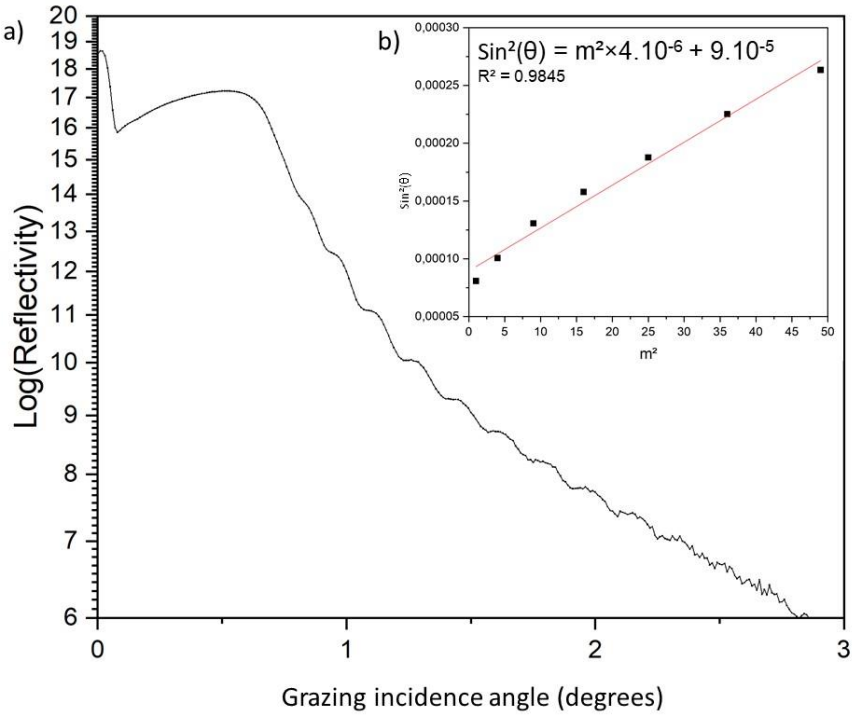

SUPPORTING INFORMATION

FIGURE S4: SPECTROSCOPIC ELLIPSOMETRY EQUATIONS $\boldsymbol{n(\omega)}$ $\boldsymbol{and}$ $\boldsymbol{k(\omega)}$

$$n(\omega) = n_{\infty} + \frac{B(\omega-\omega_j)+C}{(\omega-\omega_j)^2+\Gamma_j^2}$$

$$\mathrm{K}(\omega) = \begin{cases} \frac{f_j(\omega-\omega_j)^2}{(\omega-\omega_j)^2+\Gamma_j^2}, & \omega > \omega_g \\ 0, & \omega \leq \omega_g \end{cases}$$

Where $B = \frac{f_j}{\Gamma_j}\left(\Gamma_j^2 - (\omega-\omega_j)^2\right)$ and $C = 2f_j\Gamma_j(\omega_j - \omega_g)$

SUPPORTING INFORMATION

Figure S5: (a) AFM topographic, (b) phase PFM and (c) amplitude PFM images simultaneously recorded on the PrWO thin film surface where artificial domains were locally induced by applying DC voltages of +10 and -10 V to the AFM tip over rectangular area at the free surface of the film. Strong contrasts observed on both phase and amplitude PFM images reveal the efficient local switching of the ferroelectric domains. The AFM surface morphology simultaneously recorded with PFM images does not evidence any change on the surface, which excludes surface electrochemical processes during the writing step and supports the ferroelectric switching of the polarization.

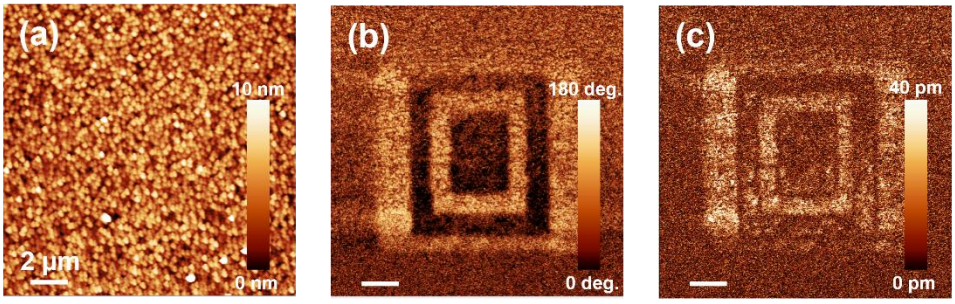

FIGURES

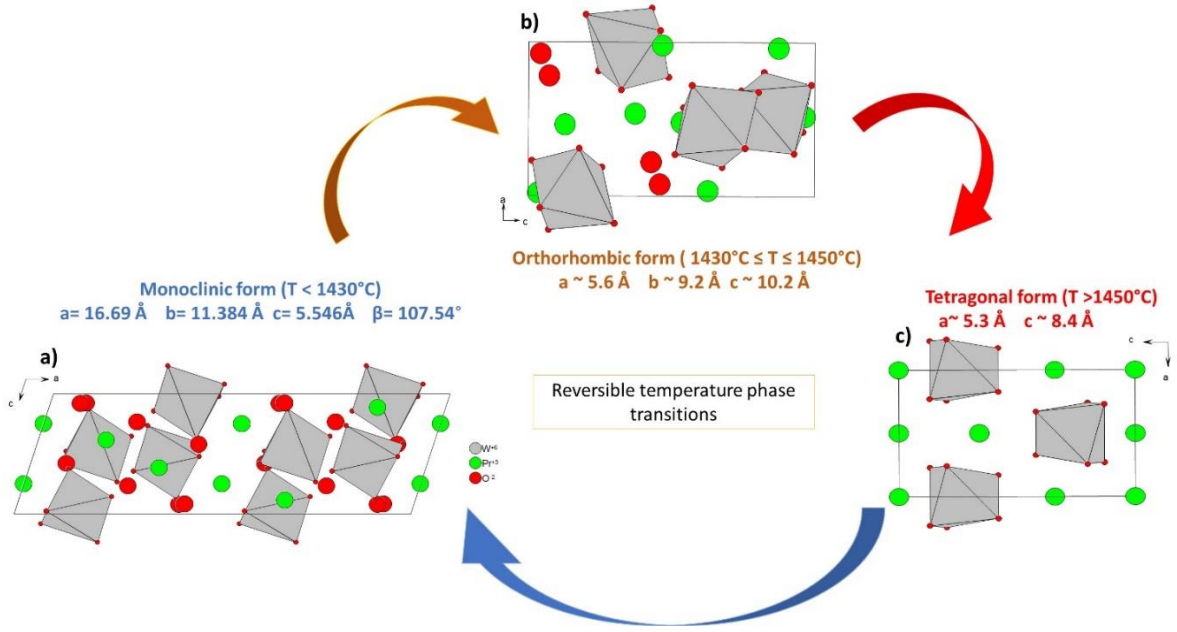

Figure 1: Temperature dependence of Pr_2WO_6 bulk structure. The three polymorph structure projections are drawn: (a) low-temperature monoclinic polymorph with isolated [WO_6] octahedra; (b) orthorhombic intermediate-temperature polymorph showing also [WO_6] octahedra and c) high-temperature tetragonal Pr_2WO_6 form as evocated by Yoshimura. [30]

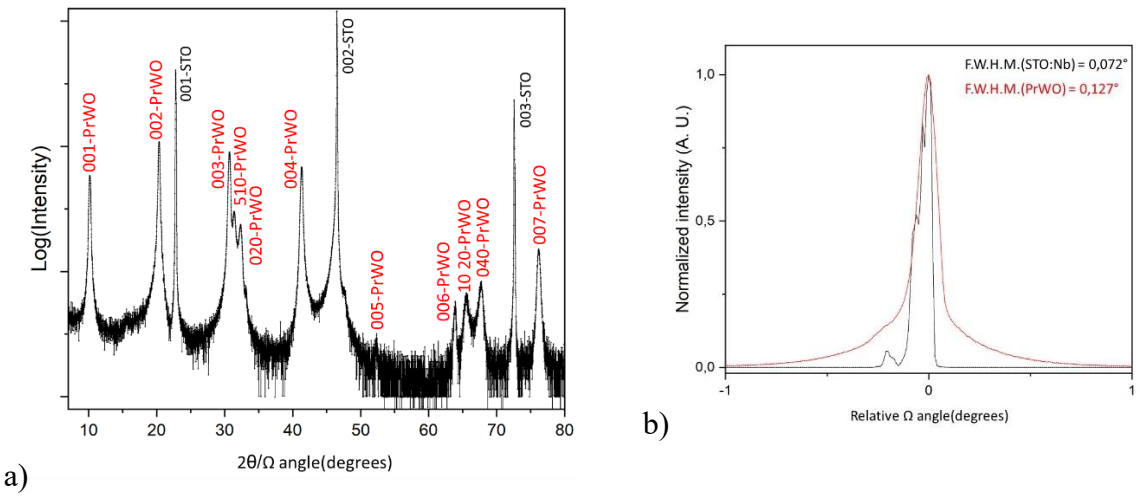

Figure 2: a) 2θ-ω X-ray diffractogram of the thin film PrWO and the substrate Nb:STO (001)-oriented; b) The rocking curves on the 001-STO substrate and the 002-thin film peak diffractions

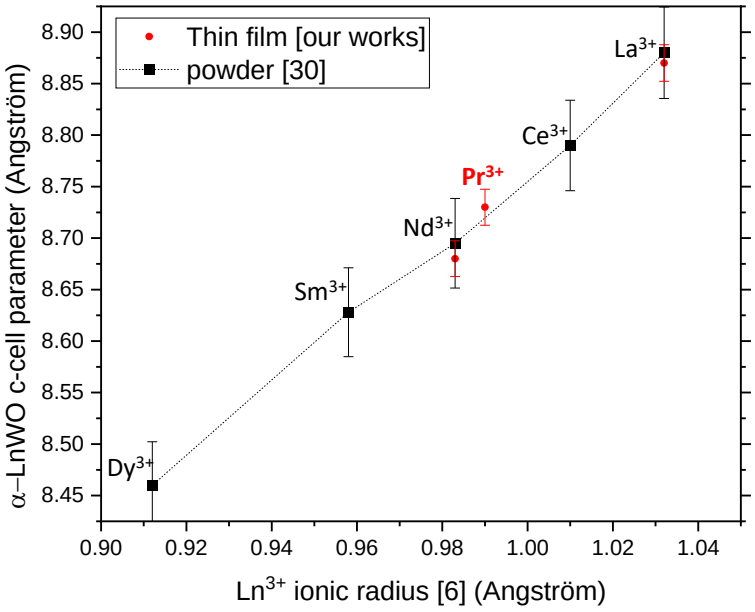

Figure 3: *c*-cell parameter dependance with Ln^{3+} ionic radius in coordinance [6] for α-Ln_2WO_6. In black: Yoshimura's results on quenched powders; [30] In red: our results on thin films. [16; 17]

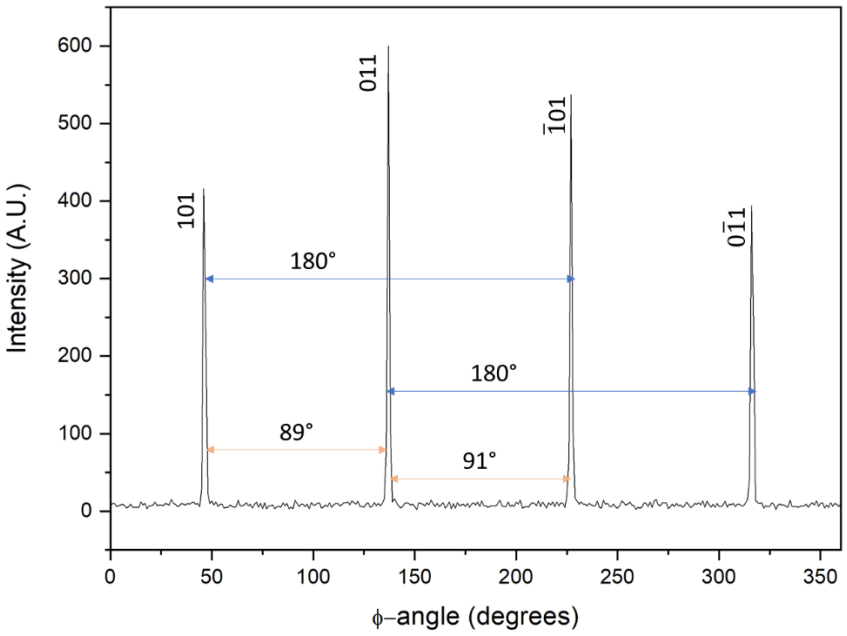

Figure 4: Phi-Scan for the thin film PrWO on the 101 and 011 diffraction peaks. The peak repetition rate is 180° showing the maximal symmetry order of 2.

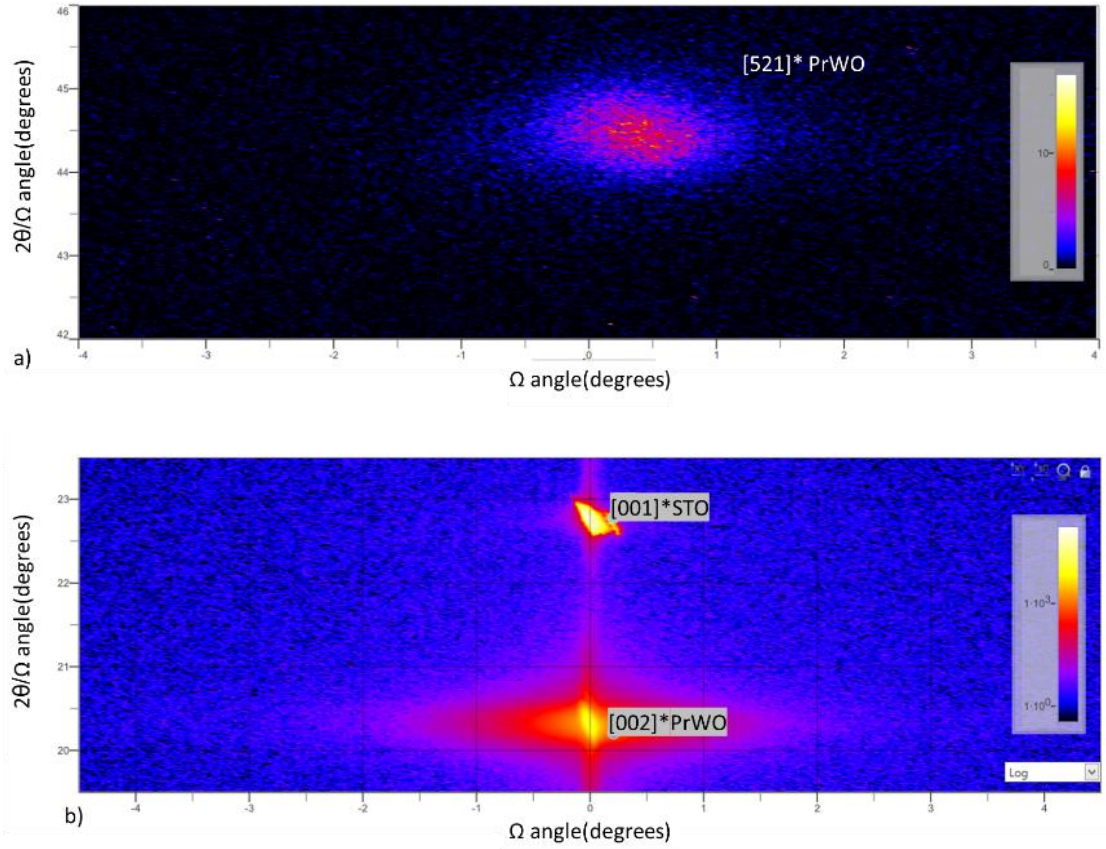

Figure 5: a) Reciprocal Space Maps along a) the [521]* α-PrWO thin film direction and b) The [001]* STO substrate and the [002]* α-PrWO thin film directions

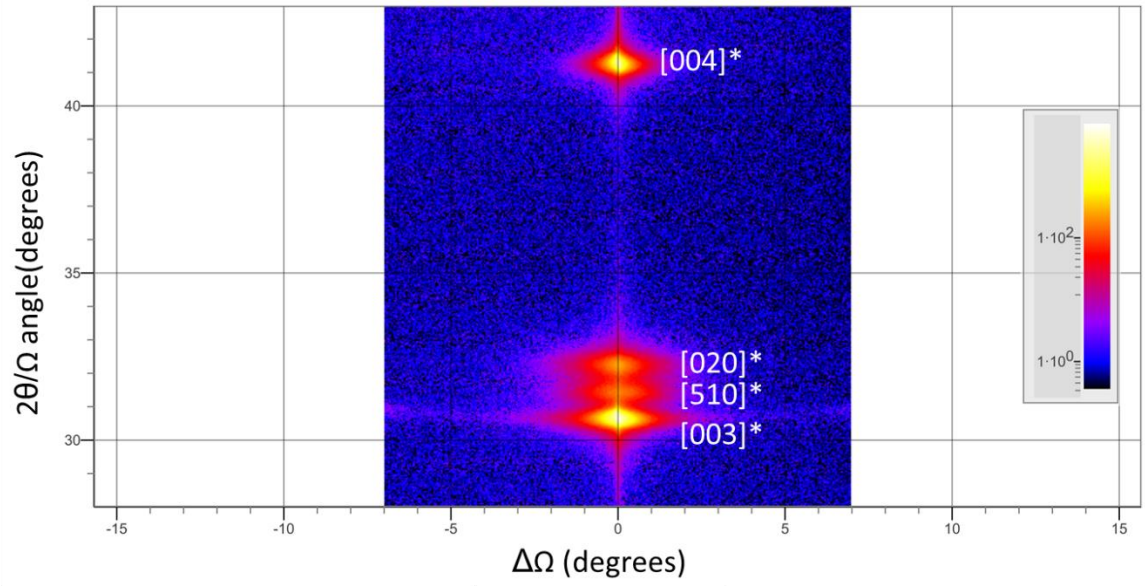

Figure 6: Reciprocal spatial maps along the [003]*, [510]* , [020]* and [004]* directions of the α-PrWO thin film.

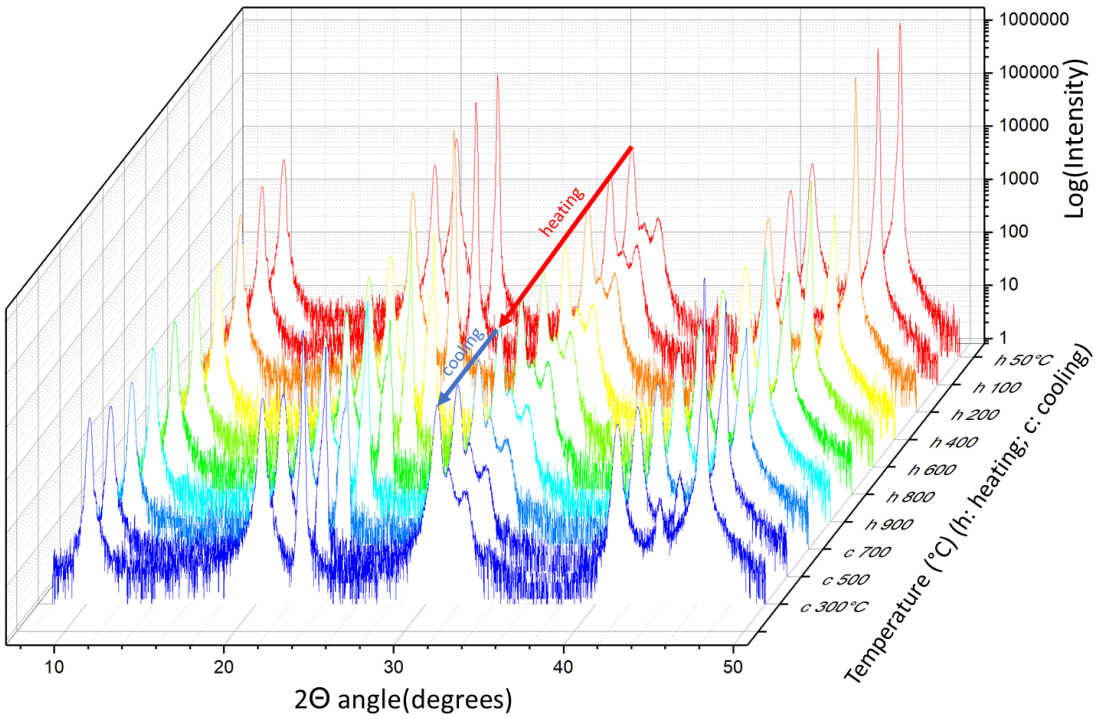

Figure 7: *In situ* thin film X-Ray diffractograms at temperatures of 50-900°C (h: heating) and 900-300°C (c: cooling)

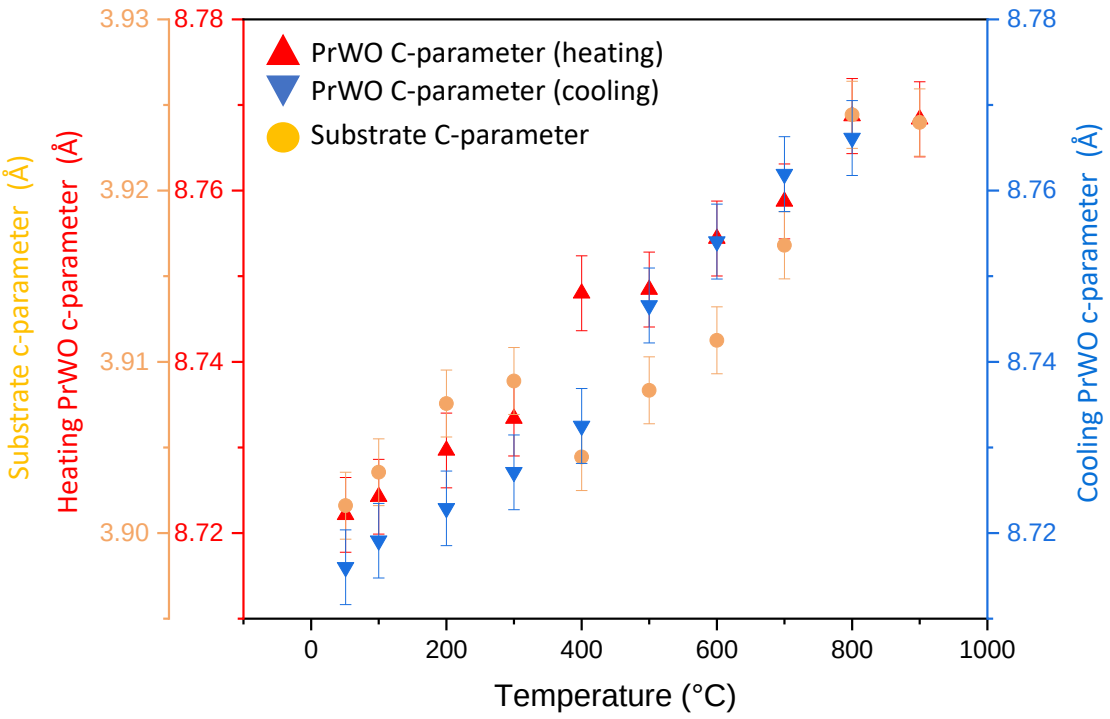

Figure 8: Evolutions of *c*-cell parameters at temperatures of 50-900°C and 900-300°C: In red (heating) and blue (cooling) for the thin film and in orange for the substrate.

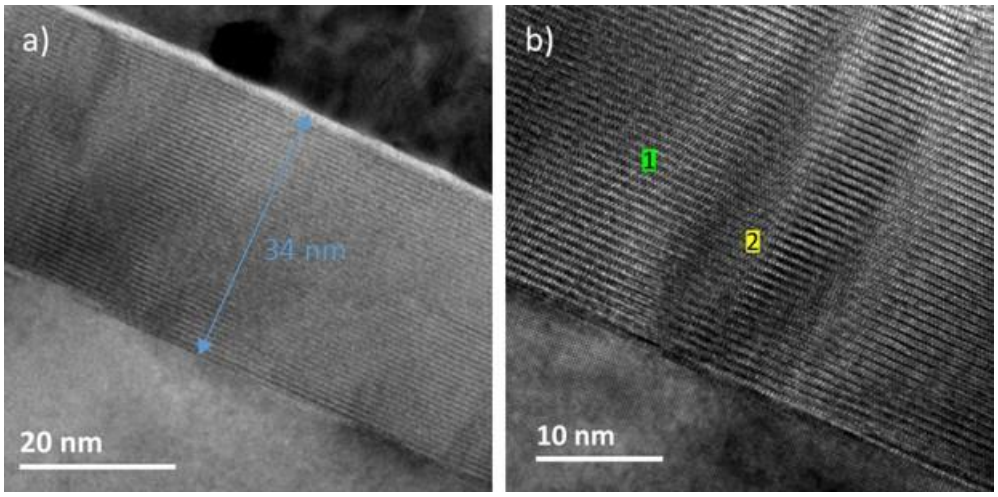

Figure 9: a) & b) HRTEM images of the layer and the substrate at different scales and sample zones

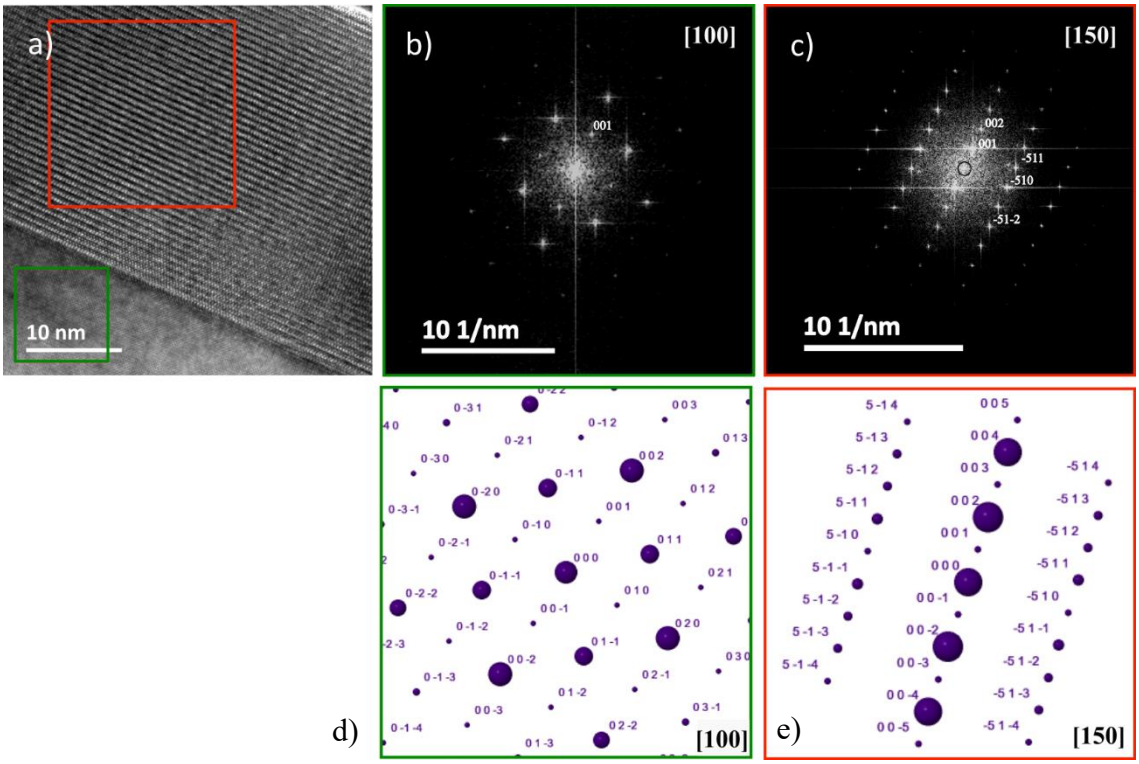

Figure 10: HRTEM image of the PrWO layer and the STO substrate (a) with corresponding FFTs for the substrate (b) (green, in [100] zone axis) and layer (c) (red, in [150] zone axis). The theoretical dynamic diffraction patterns (d) and (e) used for the indexation are shown below.

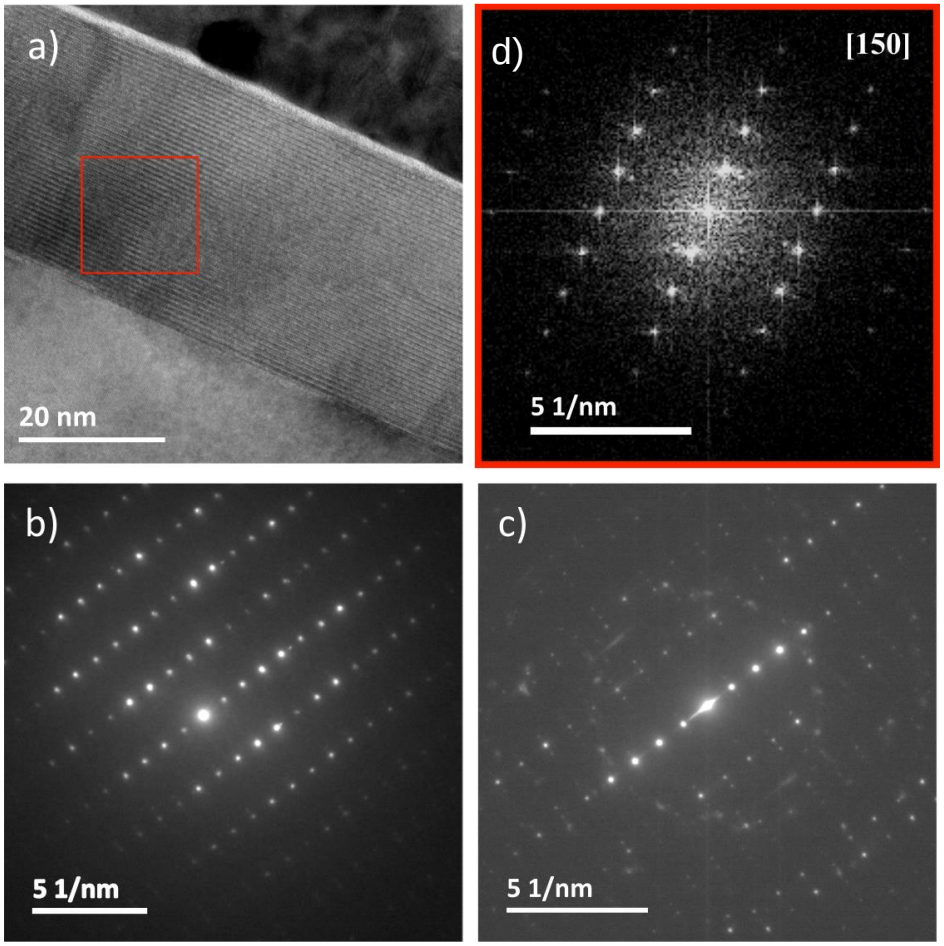

Figure 11: HREM image (a) and corresponding FFT (b) of the PrWO layer. c) and d) are nano-beam diffraction (NBD) patterns where satellite spots in the $[\bar{5}10]$ direction are observed indicating a superstructure at $\frac{1}{6}$. Note that the ring diffraction arises from the Au protective layer deposited on top of the sample for FIB lamella preparation.

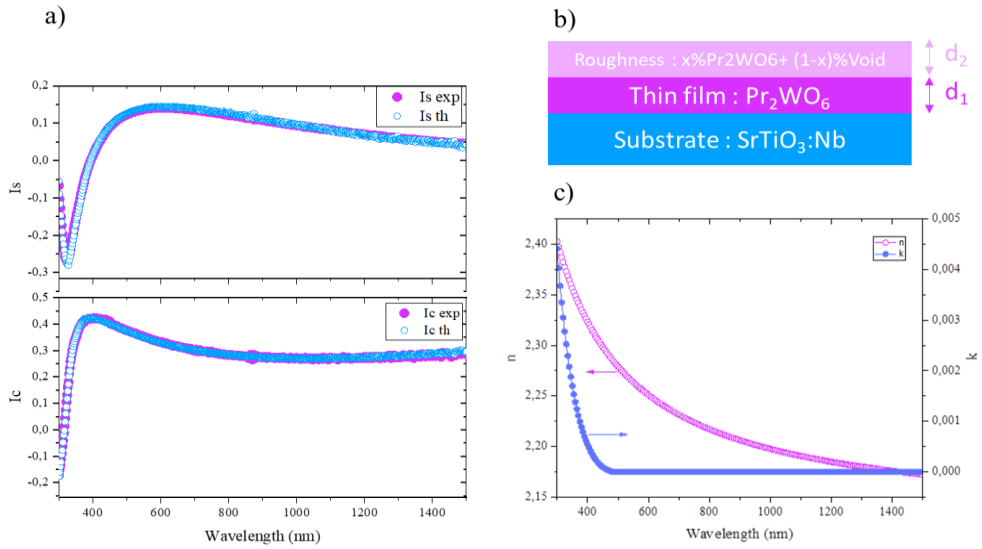

Fig. 12: a) Example of results of the I_s and I_c curves for the PrWO thin film. Filled and open circles represent the experimental and calculated data, respectively. b) Three-layers model used for ellipsometric modelling c) Refractive index and extinction of PrWO after modelling.

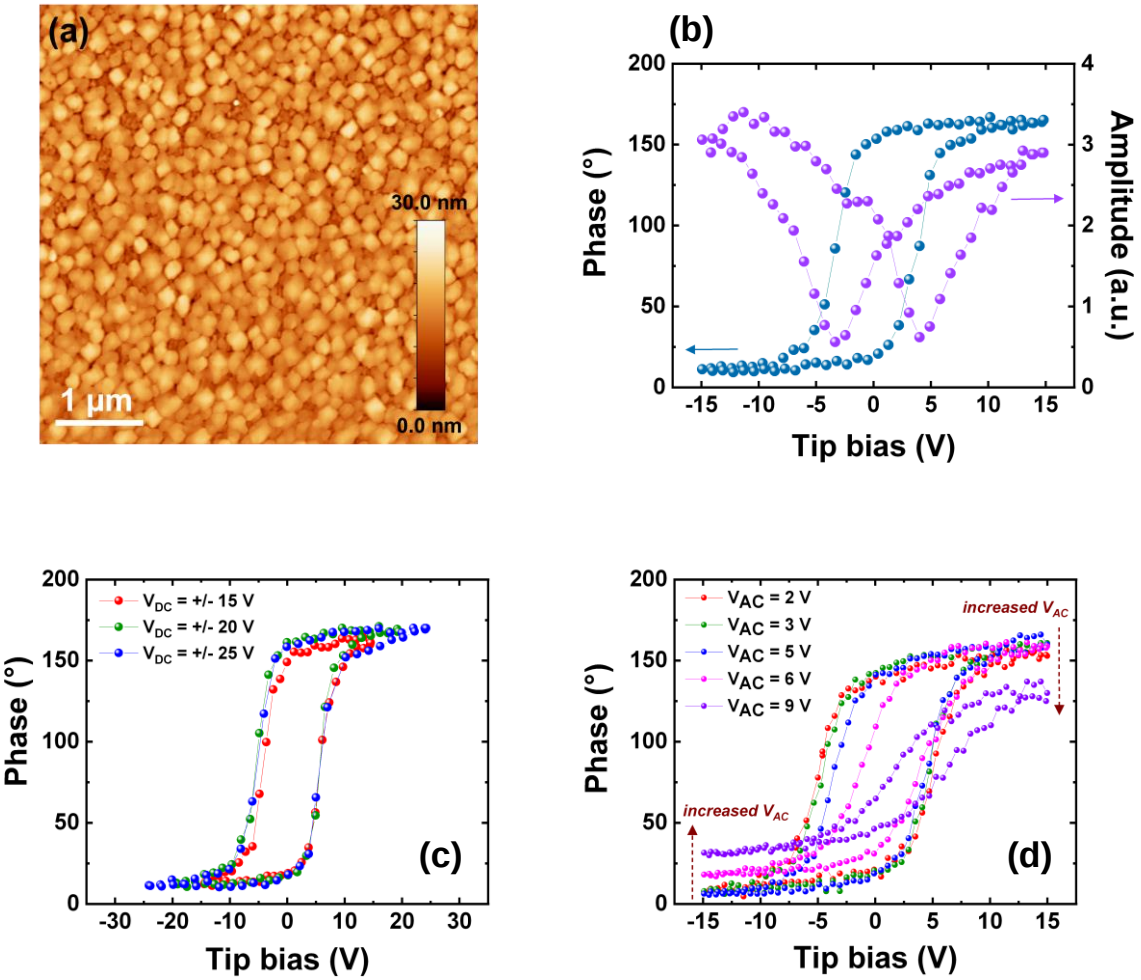

Figure 13: Nanoscale morphological and electrical properties of the PrWO thin film. (a) AFM surface morphology. (b) Remnant phase and amplitude PFM loops. Phase PFM loops under (c) different DC applied voltages and (d) different AC driving voltages.

ASSOCIATED CONTENT

AUTHOR INFORMATION

Corresponding Author

*mhelene.chambrier@univ-artois.fr

Author Contributions

The manuscript was written through contributions of all authors. All authors have given approval to the final version of the manuscript. ‡These authors contributed equally. (match statement to author names with a symbol)

ACKNOWLEDGMENT

Chevreul Institute (FR 2638), Ministère de l'Enseignement Supérieur, de la Recherche et de l'Innovation, Hauts-de-France Region, Fonds Européen de Développement Régional (FEDER) and Major Domain of Interest (DIM) ''Eco-Energy Efficiency'' of Artois University are acknowledged for supporting and funding partially this work. Région Hauts-de-France and FEDER are acknowledged for funding the MFP-3D microscope under the Program ''Chemistry and Materials for a Sustainable Growth''.

REFERENCES

[1] Directive 2002/95/EC of the European Parliamant and of the Council of 27 January 2003 on the restriction of the use of certain hazardous substances in electrical and electronic equipment, *Official Journal of the European Union* L37 (2003), 19-23.

[2] Corrigendum to Regulation (EC) N° 1907/2006 of the European Parliament and of the Council of 18 December 2006 concerning the Registration, Evaluation, Authorisation and Restriction of Chemicals (REACH), establishing a European Chemicals Agency, amending Directive 1999/45/EC and repealing Council Regulation (EEC) N° 793/93 and Commission Regulation (EC) N° 1488/94 as well as Council Directive 76/769/EEC and Commission Directives 91/155/EEC, 93/67/EEC, 93/105/EC and 2000/21, *Official Journal European Union* L136, **2007** , 3-280.

[3] Rödel, J.; Li, J.-F. Lead-free piezoceramics: Status and perspectives, *MRS Bulletin* **2018**, 43 (8), 576-580.

[4] Condoo, I.; Panwar, N.; Kholkin, A. Lead-free piezoelectrics: Current status and perspectives, *Journal of Advanced Dielectrics* **2013**, 3 (2), 1330002.

[5] Liu, W.; Ren, X. Large piezoelectric effect in Pb-free ceramics, *P. R. L.*, **2009**, 103, 257602

[6] Günter, P. Piezoelectric tensor of $KNbO_3$, *Jpn J. Appl. Phy*s. **1977**, 16 (9), 1727-1728.

[7] Jaeger, R.E.; Egerton, L. Hot pressing of potassium-sodium niobates, *J. of Am. Ceram. Soc.* **1962**, 45 (5), 209-213.

[8] Smolenskii, G.A.; Agranovskya, A.I.; Isupov, S.V; Isupov, V.A. New ferroelectrics of complex composition, *Sov. Phys., Sol. Stat.* **1961**, 2 (11), 2651-2654.

[9] Chen, M.; Xu, Q.; Kim, B. H.; Ahn, B. K.; Ko, J. H.; Kang, W. J.; Nam, O. J. Structure and electrical properties of $(Na_{0.5}Bi_{0.5})_{1-x}Ba_xTiO_3$ piezoelectric ceramics, *J. Eur. Ceram.Soc.* **2008**, 28 (4), 843-849.

[10] Ramesh, R.; Spaldin, N.A. Multiferroics: Progress and prospects in thin films, *Nat.Mat.***2007**, 6, 21-29.

[11] Ranjith, R.; Mangalam, R.V.K.; Boullay, Ph.; David, A.; Lepetit, M.B.; Lüders, U.; Prellier, W.; Da Costa, A.; Ferri, A.; Desfeux, R.; Vincze, Gy.; Radi, Zs.; Aruta, C. Constrained ferroelectric domain orientation in $BiFeO_3/SrTiO_3$ heterostructures, *A. P. L.* **2010**, 96, 022902.

[12] Bruyer, E.; Sayede, A.; Ferri, A.; Desfeux, R.; Mangalam, R.V.K.; Ranjith, R.; Prellier, W. Insight on the ferroelectric properties in a $(BiFeO_3)_2(SrTiO_3)_4$ superlattice from experiment and ab initio calculations, *A. P. L.* **2015**, 107, 042904.

[13] Xu, K.; Lu, X.; Xiang, H. Designing new ferroelectrics with a general strategy. *NPJ* Quant Mater **2017**, 2, 1.

[14] Saitzek, S.; Shao, Z.; Bayart, A.; Ferri, A.; Huvé, M.; Roussel, P.; Desfeux, R. Ferroelectricity in $La_2Zr_2O_7$ thin films with a frustrated pyrochlore-type structure. *J. Mater. Chem. C* **2014**, 2 (20), 4037-4043.

[15] Carlier, T.; Chambrier, M.-H.; Ferri, A.; Estrade, S.; Blach, J.-F.; Martin, G.; Meziane, B.; Peiro, F.; Roussel, P.; Ponchel, F.; Rémiens, D.; Cornet, A.; Desfeux, R. Lead-Free α-La_2WO_6 Ferroelectric Thin Films. *ACS Appl. Mater. Interfaces* **2015**, 7, 24409-24418.

[16] Carlier, T.; Chambrier, M.-H; Ferri, A.; Bayart, A; Roussel, P.; Saitzek, S.; Desfeux, R. Microstucture and local electrical investigation of lead-free α-La_2WO_6 ferroelectric thin films by piezoresponse force microscopy. *Thin Solid Films* **2016**, 639, 841-851.

[17] Carlier, T; Chambrier, M.-H.; Da Costa, A.; Blanchard, F.; Denneulin, T.; Létiche, M.; Roussel, P.; Desfeux, R.; Ferri, A. Ferroelectric State in an α-Nd_2WO_6 Polymorph Stabilized in a Thin Film. *Chem. Mater.* **2020**, 32 (317), 7188-7200.

[18] Yoshimura, M. High temperature phase relation in the system La_2O_3-WO_3. *Mat.Res.Bull.* **1976**, 11 (2), 151-158.

[19] Efremov, V. A. Characteristic features of the crystal chemistry of lanthanide molybdates and tungstates. *Russ. Chem. Rev.* **1990**, 59, 627-642.

[20] Borchardt, H. J. Rare-Earth Tungstates and 1:1 Oxytungstates. *J. Chem. Phys.* **1963**, 39, 504.

[21] Brixner, L. H.; Sleight, A. W.; Foris, C. M. Refined Cell parameters of the Ln_2WO_6-Type Rare Earth Tunsgates. *J.S.S.C.* **1973**, 7, 418.

[22] Wyart, J.; Klevtsov, P. V.; Kharchenko L. Y.; Polanskaya, T. M. Synthèse et étude cristallographique des oxytugstates Ln_2WO_6 avec Ln = Pr et Nd. *Bull. Soc. Française et de cristallographie* **1970**, 93 (5-6), 536-538.

[23] Shimazaki, T.; Yamazaki, T.; Terayama, K.; Ishiguro, T.; Yoshimura, M. Investigation of double oxides in the system of Pr_2O_3-WO_3. *J. Alloys & Compounds* **1999**, 285, 112-118.

[24] Kaczmarek, S. M.; Tomaszewicz, E.; Moszynski, D.; Jasik, A.; Leniec, G. DTA/TG, IR, EPR and XPS studies of some praseodynium (III) tungstates. *Mat. Chem. & Phys.* **2010**, 124, 646-651.

[25] Reznik, E., Ivanova., *Russ. J. Inorg. Chem. (Engl. Transl.)* **1976**, 21, 281.

[26] Rodriguez, B.J.; Callahan, C.; Kalinin, S. V., Proksch, R. Dual-frequency resonance tracking atomic force microscopy. Nanotechnology **2007**, 18, 1-6.

[27] Qiao, H., Seol, D.; Sun, C.; Kim, Y. Electrostatic contribution to hysteresis loop in piezoresponse force microscopy. *Appl. Phys. Lett.* **2019**, 114, 152901.

[28] Allix, M.; Chambrier, M. H.; Veron, E.; Porcher, F.; Suchomel, M.; Goutenoire, F. Synthesis and Structure Determination of the High Temperature Form of La_2WO_6. *Cryst. Growth Des.* **2011**, 11(6), 2528-2539.

[29] Shannon, R. D. Revised effective ionic radii and systematic studies of interatomic distances in halides and chalcogenides. *Acta Cryst.* **1976**, A32, 751.

[30] Yoshimura, M; Rouanet, A.; Sibieude, F.; Foex, M. Phases de haute température des tungstates de lanthanides du type Ln_2O_3-WO_3 (Ln = La, Ce, Nd, Sm, Dy et Y). *C. R. Acad. Sci. C. Fr*. **1974**, 279, 863-865.

[31] Salzmann, I; Stereopole version 1.2 X-Ray Pole Figure Analysis with IDL: software CaRIne **2004**

[32] Scott, N.H. Thermoelasticity with thermomechanical constraints. *International Journal of Non-Linear Mechanics* **2001**, 36 (3), 549-564.

[33] Feutmba, G. F.; Hermans, A.; George, J. P.; Rijckaert, H.; Ansari, I.; Van Thourhout, D.; Beeckman, J. Reversible and Tunable Second-Order Nonlinear Optical Susceptibility in PZT Thin Films for Integrated Optics. *Adv. Optical Mat.* **2021**, 9, 2170062.

[34] Vasudevan, R. K.; Balke, N.; Maksymovych, P.; Jesse, S.; Kalinin, S. V. Ferroelectric or non-ferroelectric: Why so many materials exhibit "ferroelectricity" on the nanoscale. *Appl. Phys. Lett.* **2017**, 4, 021302.

[35] Chen, Q. N.; Ou, Y.; Ma, F.; Li, J. Mechanisms of electromechanical coupling in strain based scanning probe microscopy. *Appl. Phys. Lett.* **2014**, 104, 242907.

[36] Strelcov, E.; Kim, Y.; Yang, J. C.; Chu, Y. H.; Yu, P.; Lu, X.; Jesse, S.; Kalinin, S. V. Role of Measurement Voltage on Hysteresis Loop Shape in Piezoresponse Force Microscopy. *Appl. Phys. Lett.* **2012**, 101, 192902.

[37] Balke, N.; Maksymovych, P.; Jesse, S.; Herklotz, A.; Tselev, A.; Eom, C.-B.; Kravchenko, I. I.; Yu, P.; Kalinin, S. V. Differentiating Ferroelectric and Nonferroelectric Electronmechanical Effects with Scanning Probe Microscopy. *ACS Nano* **2015**, 9, 6484−6492.

[38] Collins, L.; Liu, Y.; Ovchinnikova, O. S.; Proksch, R. Quantitative Electromechanical Atomic Force Microscopy. *ACS Nano*. **2019**, 13, 8055–8066

[39] Gruverman, A.; Alexe, M.; Meier, D. Piezoresponse force microscopy and nanoferroic phenomena. *Nat. Commun.* **2019**, 10, No. 056502.